Energy Advances

Modeling as the Bridge to Net Zero

ROYAL SOCIETY
OF CHEMISTRY

PAPER
Martin van Sint Annaland *et al.*
Purity-constrained TVSA modeling of Lewatit VPOC 1065
for direct air capture: bridging cured thermodynamics,
process design and geometrical analysis

ROYAL SOCIETY
OF CHEMISTRY

PAPER

Check for updates

Purity-constrained TVSA modeling of Lewatit VPOC 1065 for direct air capture: bridging cured thermodynamics, process design and geometrical analysis

Mattia Galanti, [iD] Kiia Kaaresvirta, Ivo Roghair and Martin van Sint Annaland*

Direct air capture (DAC) is a leading carbon dioxide removal (CDR) technology that extracts CO_2 directly from ambient air, independent of emission sources. Among the various process designs, temperature–vacuum swing adsorption (TVSA) has emerged as the most mature technology and is currently deployed at commercial scale, particularly in its steam-assisted configuration. However, the DAC-TVSA process has often been evaluated using incomplete models, where critical aspects such as the O_2 purity constraint were ignored or the condenser energy cost was neglected, potentially leading to misleading feasibility assessments. This work develops a comprehensive TVSA modeling framework that unifies detailed adsorption thermodynamics for both dry and humid conditions, refined heat-transfer descriptions accounting for wall-driven regeneration, realistic treatment of auxiliary equipment, and explicit oxygen-purity constraints. The model was benchmarked against literature data, demonstrating that the omission of stricter process constraints can severely underestimate the actual energy–productivity trade-offs. Additionally, the study identified the pre-heating step required to meet the O_2 specification as the critical bottleneck in both wall-heated and steam-assisted configurations. The impact of this limitation was further analyzed by systematically varying the adsorber aspect ratio. This revealed the existence of an optimal region, governed by the trade-off between enhanced heat transfer in flatter geometries and increased pressure drop associated with longer beds. In parallel, the benefits of steam injection were visualized through minimum work envelopes, which clearly highlighted the performance gains achievable by improving the desorption step. Overall, the results highlight the substantial potential that can be realized by directly addressing the critical bottlenecks of DAC.

1 Introduction

Global CO_2 emissions have risen steadily since the industrial era, driving climate change and severe environmental impacts. Average temperatures are already 1.1 °C above 1850–1900 levels and will continue to increase without rapid mitigation.[1] Since the launch of the UN Framework Convention on Climate Change in 1992, emissions have grown by 60%.[2] In response, the 2015 Paris Agreement set the critical target of limiting warming to 1.5 °C by 2100.[3,4] Meeting climate goals demands both deep emission cuts and large-scale deployment of negative emission technologies (NETs) to offset residual emissions from hard-to-abate sectors such as aviation, agriculture, and heavy industry.[5]

Direct air capture (DAC) is a leading carbon dioxide removal (CDR) technology that extracts CO_2 directly from ambient air,

Department of Chemical Engineering and Chemistry, Eindhoven University of Technology, Eindhoven 5600MB, The Netherlands.
E-mail: M.v.SintAnnaland@tue.nl

independent of emission sources. The captured carbon can either be sequestered or converted into valuable products through hydrogen-based pathways.[6–8] To achieve net zero emissions (NZE), the International Energy Agency projects DAC deployment to rise from negligible levels today to 85 Mt CO_2 annually by 2030 and nearly 1 Gt by 2050.[9,10]

Amine-functionalized solid sorbents are among the most investigated materials for adsorption-based DAC, offering strong CO_2 affinity under ambient conditions, low-temperature regeneration, and competitive capture costs.[11] Recent work shows that well-optimized temperature–vacuum swing adsorption (TVSA) processes can surpass absorption-based approaches in both energy efficiency and productivity.[12] One of the benchmark sorbents frequently considered in the literature is Lewatit VPOC 1065 (referred to in the text as "Lewatit" for conciseness), a commercially available amine-functionalized anion exchange resin (AER) with notable capture capacity under DAC conditions. Structurally, it is a cross-linked polystyrene–divinylbenzene polymer functionalized with benzylamine

groups.[13] Veneman *et al.* (2015) were among the first to study its CO_2 adsorption behavior, focusing on post-combustion applications.[14] Later, Sutanto *et al.* extended the analysis to biogas upgrading.[15] Bos *et al.* advanced this work by investigating intrinsic adsorption kinetics and expanding the isotherm dataset across additional temperatures.[16] The first application of Lewatit VPOC 1065 to DAC was reported by Young *et al.*, who provided a comprehensive experimental and modeling framework including both dry/wet isotherms and TVSA process optimization.[17] Subsequent studies further refined the thermodynamic picture: Low *et al.* measured low-pressure isotherms under DAC-relevant conditions, while Shi *et al.* and Petersen *et al.* investigated adsorption kinetics and performed breakthrough experiments for packed-bed adsorption.[18–20]

Assessing the feasibility and scalability of DAC requires detailed TVSA process modeling to capture system behavior under practical operating conditions.[21] Yet, reliable simulation remains challenging. In particular, several critical aspects complicate the development of accurate models.

Adsorption isotherms often deviate from ideal behavior and exhibit strong CO_2–H_2O co-adsorption effects, which are nontrivial to capture with reported models in the literature. Moreover, thermodynamic data are often found with significant variations and discrepancies between scientific articles, leading to large variations in predicted energy requirements and capture performance.[22]

Heat transfer strongly influences regeneration efficiency and is rarely modeled with sufficient detail, often using simple models that neglect the radial contribution to heat transfer, crucial in process configurations where desorption energy is delivered to the bed radially through the walls. A similar situation holds for auxiliary process equipment, such as condensers and vacuum pumps, which can significantly impact overall energy consumption.

Moreover, oxygen contamination limits impose strict requirements on cycle design. In fact, oxygen control is not only essential for downstream utilization to avoid compromising CO_2 transport infrastructure but also crucial to mitigate its strong oxidative degradation effect on amine sorbents, particularly under high-temperature desorption conditions.[23] Despite their importance, the effect of oxygen specifications on TVSA cycle performance has received virtually no attention in the literature, leaving a critical gap in our understanding of how purity constraints shape process operation and energy efficiency.

This work addresses these gaps by developing a comprehensive TVSA modeling framework that unifies detailed adsorption thermodynamics for both dry and humid conditions, refined heat-transfer descriptions accounting for wall-driven regeneration, realistic treatment of auxiliary equipment, and explicit oxygen-purity constraints. By systematically incorporating these elements, we reveal how current simplifications in the literature may lead to misleading feasibility assessments and provide a more robust picture of the true performance and scalability potential of DAC systems.

2 Thermodynamics

Adsorption isotherms are mathematical models used to describe the equilibrium adsorption capacity as a function of partial pressure and temperature.[24] For the reference Lewatit sorbent, a substantial amount of thermodynamic data is available in the literature, in publications published between 2015 and 2024. However, as shown in our previous work, a closer examination highlights significant discrepancies and variability among reported isotherms.[22] Achieving the most accurate possible description of adsorption thermodynamics is essential for TVSA modeling, as even moderate deviations in the isotherm shape or capacity translate into large errors in predicted energy consumption and process performance. For this reason, two complementary strategies are pursued: fitting all available data to capture the broadest possible description and filtering the dataset to retain only consistent measurements in order to obtain a more coherent and physically reliable fit.

2.1 Unary CO_2 isotherm

2.1.1 Data collection. The collection of all the available isotherm data points can be found in Fig. 1. The experimental dataset comprises a total of 638 data points, predominantly originating from the study by Low *et al.* (324 points, 50.8% of the total). The second largest contributor is the study by Sutanto *et al.* with 81 points (12.7%), followed by the studies by Petersen *et al.* (71 points, 11.1%), Shi *et al.* (57 points, 8.9%), Young *et al.* (58 points, 9.1%), Veneman *et al.* (42 points, 6.6%), and Bos *et al.* (5 points, 0.8%). Within the DAC-relevant pressure window, the dataset remains imbalanced: most data originate from the studies by Low and, to a lesser extent, Shi and Petersen, while other sources contribute only marginally. In addition, as highlighted in our recent analysis, the coverage across temperatures is sparse and irregular, while deviations between sources can be observed homogeneously among all temperatures, particularly pronounced in the high CO_2 partial pressure range.[22]

2.1.2 Isotherm fitting. The most common model used to fit unary CO_2 isotherm data is the temperature-dependent Toth
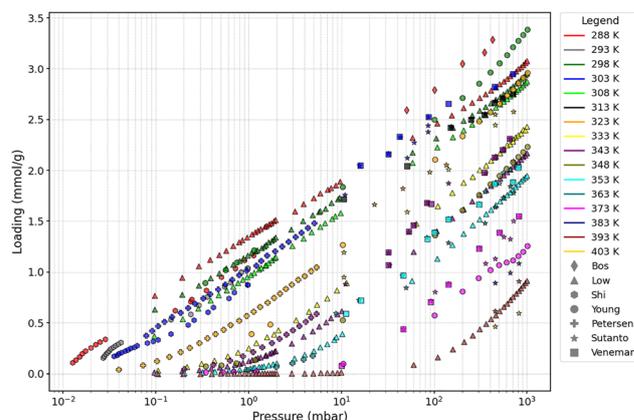

Fig. 1 Experimental unary CO_2 adsorption isotherms reported in the literature, covering multiple temperatures and sources.

model (eqn (1)). In this work, we adopted the Toth model as a pragmatic and parsimonious reference model to describe and summarize the joint literature datasets. Its simplicity and widespread use in adsorption studies make it a suitable baseline for comparing data across different sources, while acknowledging that deviations may occur where experimental uncertainties become more pronounced.

The full model involves seven parameters to be fitted from experimental isotherm data: q_∞, χ, b_0, ΔH_{st}^0, τ_0, β, and T_0, where q_∞ is the maximum adsorption capacity, b_0 is the affinity at the reference temperature T_0, and ΔH_{st}^0 is the isosteric heat of adsorption at zero loading, while χ, τ_0 and β are empirical parameters.[24] Typically, the reference temperature T_0 is fixed *a priori*, while χ is usually set to zero, enforcing that the maximum number of adsorption sites in Lewatit does not decrease with temperature. Thus, the actual number of parameters to be obtained by fitting reduces to five,

$$q_{eq(P,T)} = q_{m(T)} \frac{b_{(T)}P}{\left(1 + \left(b_{(T)}P\right)^{\tau_{(T)}}\right)^{\frac{1}{\tau_{(T)}}}} \qquad (1a)$$

$$q_{m(T)} = q_\infty \exp\left[\chi\left(1 - \frac{T}{T_0}\right)\right] \qquad (1b)$$

$$b_{(T)} = b_0 \exp\left[\frac{\Delta H_{st}^0}{R_{gas}T}\left(\frac{T_0}{T} - 1\right)\right] \qquad (1c)$$

$$\tau_{(T)} = \tau_0 + \beta\left(1 - \frac{T_0}{T}\right) \qquad (1d)$$

However, when applied to the complete set of literature data, the model does not provide a satisfactory description, as illustrated in Fig. S1 (SI). As discussed in the study by Galanti *et al.* (2025), the Toth model cannot simultaneously capture all datasets with equal accuracy across the full pressure range, reflecting both its intrinsic functional limitations and experimental variability among sources.[22] To ensure internal consistency, we assessed the mutual coherence of each dataset rather than its absolute agreement with the model:

• The measurements reported by Shi *et al.* contain points at extremely low CO_2 partial pressures (0.01–0.1 mbar) which display trends that differ from the other datasets, not only in magnitude but also in shape (curvature) in log-p space. This mismatch may reflect the intrinsic challenges of generating reliable adsorption data under such dilute conditions, where measurement uncertainty and noise are more pronounced. Additionally, the Toth model might be unable to accurately describe those points. In fact, as discussed in the study by Galanti *et al.* (2025) and highlighted in Fig. S2 in the SI, residual-*vs.*-fit plots show clustered negative residuals at low loadings (model overestimation) and a curvature mismatch, consistent with a structural limitation of the Toth functional form. A revised analysis with additional details can be found in the SI.

Following a model-independent perspective, between 0.1 and 10 mbar, the data from the study by Shi *et al.* deviate

from the rest. In fact, at 288 K (where only data from the studies by Low and Shi are available), the data from the study by Shi remarkably disagree with those from the study by Low, and at 303 K, data also deviate from those from the study by Petersen. However, data from the studies by Low and Young closely agree at 298 K. Data from the studies by Petersen and Low show a slight deviation at 343 K, while data from the studies by Petersen and Young appear to deviate at 323 K. The latter mismatch is likely due to measurement errors in the two lowest-pressure points of Young's dataset, as these align well with the rest of the data at higher pressures. Given the 298 K Low–Young cross-validation, the consistent agreement among the remaining datasets, and acknowledging that including anomalous data at ultra-low pressures would bias parameter estimation and degrade the overall quality of the isotherm model, the measurements from the study by Shi *et al.* were removed from the dataset.

• In the higher-pressure region (10–1000 mbar), a similar consistency check was performed. In this range, data from from the study by Low *et al.* begin to systematically deviate from the other datasets, underestimating the loading across the entire interval, as highlighted in Fig. S3 in the SI. In contrast, the remaining datasets, though not accurately reproduced by the Toth model in absolute terms, exhibit mutually consistent residual patterns, indicating that they respond coherently within the model's structural limitations. The residual distribution analysis reported in the SI confirms this observation: data from the study by Low show a statistically significant deviation from all other sources, whereas data from the studies by Young, Sutanto, and Veneman display comparable residual distributions within model uncertainty. This indicates that the divergence originates from dataset-specific bias rather than from a structural limitation of the model. Consequently, the high-pressure subset from the study by Low *et al.* was excluded, whereas their low-pressure data were retained due to close cross-validation with data from the study by Young *et al.* under overlapping conditions. The detailed statistical comparison supporting this decision is provided in the SI.

Given the significant scatter and inconsistencies across published unary CO_2 isotherm datasets, directly adopting any single literature source would inevitably introduce implicit bias toward specific authors or measurement techniques. For this reason, we curated the compiled database by prioritizing mutual coherence between independent datasets, rather than absolute agreement with any individual study. This procedure results in a more internally consistent reference dataset, providing a bias-minimized and more representative "reference-average" adsorption description. The fitting results of the Toth model referring to the new curated dataset ("selected data") are presented in Fig. 2. A better general description is obtained compared to the "all data" dataset, both qualitatively and quantitatively, as shown in Table 1, where the root mean squared error (RMSE) and mean absolute error (MAE) fitting error metrics are presented (definitions are available in the SI) (Table 2).
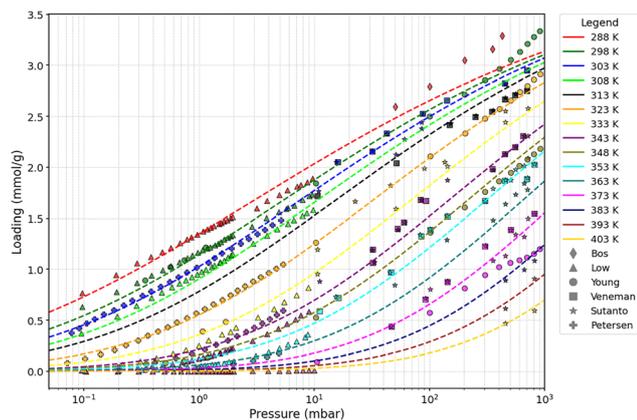
Fig. 2 Unary CO_2 adsorption isotherm Toth fit using selected data sources.

Table 1 Comparison of error metrics obtained for the Toth isotherm fit using the complete dataset and the selected dataset

Dataset	RMSE (mmol g^{-1})	MAE (mmol g^{-1})
All data	0.1114	0.0889
Selected data	0.0881	0.0671

Table 2 Optimized parameters of the Toth isotherm model for the selected dataset

Parameter	Value	Unit
$q_{sat,0}$	4.078	mmol g^{-1}
b_0	307.59	mbar^{-1}
ΔH_0	104 935	J mol^{-1}
τ_0	0.222	—
α	0.548	—

2.2 Unary H_2O isotherm

2.2.1 Data collection. H_2O isotherm data points for the Lewatit sorbent were gathered from three main sources: from the studies by Low *et al.*, Young *et al.*, and Wilkins *et al.*, and can be seen in Fig. 3. While the data from the studies by Low and Young refer to humid air in the 15–70 °C range, the measurements reported by Wilkins *et al.*[25] correspond to pure steam at 110 °C. Because steam-phase isotherms for this sorbent had not been reported prior to Wilkins *et al.*, assembling a dataset that spans both humid air and steam provides a more complete basis for model development, enabling a more reliable and accurate description of H_2O adsorption across the operating conditions.

In total, 260 points were collected (180 adsorption and 80 desorption). For adsorption, the study by Low contributes 115 points (63.9%), Young 60 (33.3%), and Wilkins 5 (2.8%); for desorption, from the study by Low contributes 60 points (75.0%), Young 12 (15.0%), and Wilkins 8 (10.0%). The only temperature at which multiple authors shared measurements is 25 °C, also providing a good correspondence between the sources.

As first reported by Veneman *et al.*, H_2O adsorption on Lewatit is a strong function of relative humidity, with a weaker
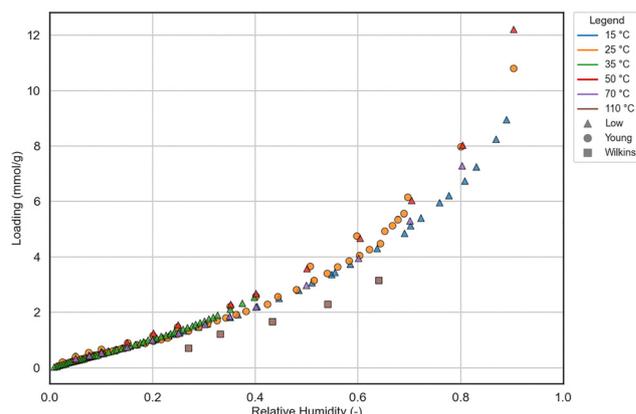

Fig. 3 Unary H_2O adsorption isotherms, covering multiple temperatures and sources.

dependence on temperature.[14] Moreover, the system is characterized by a pronounced hysteresis behavior, highlighted in Fig. S4 of the SI.

2.2.2 Isotherm fitting. The water adsorption onto the Lewatit sorbent follows closely a type III isotherm behavior following the IUPAC classification, characterized by multi-layer adsorption.[26] One of the most common models used to predict these types of systems is the Guggenheim–Anderson–de Boer model, an extension of the BET isotherm valid for high relative humidity values. The sets of equations in the Anderson derivation form are shown in eqn (2),[17,27,28]

$$q_{eq}(x, T) = q_m \frac{k(T)c(T)x}{[1 - k(T)x][1 + (c(T) - 1)k(T)x]} \quad (2a)$$

$$k(T) = \exp\left(\frac{E_{2-9}(T) - E_{10+}(T)}{R_{gas}T}\right) \quad (2b)$$

$$c(T) = \exp\left(\frac{E_1(T) - E_{10+}(T)}{R_{gas}T}\right) \quad (2c)$$

$$E_1(T) = C - \exp(DT) \quad (2d)$$

$$E_{2-9}(T) = F + GT \quad (2e)$$

$$E_{10+}(T) = 57\,220 - 44.38T \quad (2f)$$

where q_m is the monolayer maximum loading, k and c are the temperature-dependent affinity parameters, and x is the relative humidity.

The energy terms appearing in the affinity parameters refer to the adsorption energy difference between the different formed multilayers. In particular, E_1 refers to the first monolayer, and E_{2-9} refers to the adsorption heat from the 2nd to 9th layer, while E_{10+} refers to the energy associated after the 10th layer, which can be assumed to be equal to the heat of condensation. Following the observations of Young *et al.*, the different energy terms were modeled using the empirical expression provided by the author (eqn (2d)–(2f)). Therefore, the adopted GAB model requires five parameters to be fitted with the experimental data: q_m, C, D, F, and G.

Finally, for an accurate estimation of water saturation pressure and following the approach of Wilkins et al., we employed the IAPWS 1995 Equation of State, as recommended by NIST:[25,29]

$$\ln\left(\frac{P^{\text{sat}}}{P_{\text{c}}}\right) = \frac{T_{\text{c}}}{T}\left(\beta_1\nu + \beta_2\nu^{1.5} + \beta_3\nu^3 + \beta_4\nu^{3.5} + \beta_5\nu^4 + \beta_6\nu^{7.5}\right), \tag{3}$$

where T_{c} and P_{c} refer to the H_2O critical temperature and pressure (647 K and 220.64 bar, respectively), while ν is defined as $1 - T/T_{\text{c}}$, and the regression coefficients are $\beta_1 = -7.85951783$, $\beta_2 = 1.8440825$, $\beta_3 = -11.7866497$, $\beta_4 = 22.6807411$, $\beta_5 = -15.9618719$, and $\beta_6 = 1.80122502$.

As already discussed, a pronounced hysteresis behavior is observed for H_2O isotherms on Lewatit. However, Fig. S4 clearly shows that the degree of hysteresis decreases with increasing temperature. A typical TVSA process operates with adsorption at low temperature and desorption at higher temperature. Therefore, while the adsorption branch correctly represents the loading behavior under adsorption conditions, during desorption, the difference between the two branches becomes very small. For these reasons, and considering that explicit hysteresis models would add considerable complexity without significantly improving predictive capability for overall cycle performance, we therefore fitted the GAB model only to the adsorption branch (Table 3).

2.3 Binary CO₂–H₂O isotherm

Previous studies on amine functionalized adsorbents have shown that the presence of H_2O can enhance the adsorption of CO_2.[14,17,30,31] This makes Lewatit and other amine functionalized sorbents particularly advantageous for DAC, as water is present in ambient air. The co-adsorption enhancement effect has been shown to be stronger in the low partial pressure region, which aligns well with the conditions for DAC. Conversely, it has been shown that CO_2 has little impact on H_2O adsorption, although this assumption might not be valid at high relative humidity.

Young et al. and more recently Song et al. performed a co-adsorption experiment via dynamic vapor sorption (DVS) at a RH of 80% and observed an actual decrease in mass, suggesting that the assumption that CO_2 does not influence water adsorption might not hold at high relative humidities. A change in the adsorption mechanism has been observed in the presence of water, yet the exact mechanism is unknown.

Table 3 Optimized overall parameters of the GAB isotherm model for H_2O adsorption

Parameter	Value	Unit
q_{m}	3.197	mmol g^{-1}
C	46 779.95	J mol^{-1}
D	0.023	K^{-1}
F	56 233.72	J mol^{-1}
G	42.738	J mol^{-1} K^{-1}

2.3.1 Data collection. Following the approach presented in the previous sections, motivated by the data scarcity on co-adsorption isotherms, binary adsorption data were collected from five published sources. As shown in Fig. S6, 53.8% of the data originated from two papers by Young et al. and Piscina et al. using the DVS method.[17,32] The data from the study by Piscina et al. duplicated Young's results, except for the points at RH 80%. However, these points were not included during the analysis due to their inconsistencies compared to other similar data; details can be found in the SI. The data from the studies by Chimani and Veneman via the breakthrough curve method (BT) make up 17% and 9% of the total dataset, respectively.[14,30] In conclusion, the co-adsorption dataset is unevenly distributed across the studies by different authors, as the majority of the data points were provided by two collaborating studies. This hinders the evaluation of the reliability of the data, as similar conditions are rarely repeated by different authors.

An overview of the collected data is found in Fig. S5 (SI), where isotherm points were binned in pressure intervals for visualization purposes only. Overall, the cured dataset confirms the positive effect of humidity on CO_2 adsorption onto the sorbent, highlighted by the presence of the dry condition reference. Points from different authors predict similar trends, especially in the 40 Pascal bin. Conversely, as reported in the studies by Young et al. and Piscina et al., in the high pressure bins, the effect of humidity seems to hinder CO_2 adsorption at high relative humidity values. At 55% RH, the relative change becomes marginal or even negative, which may be attributed to pore blocking effects or to measurement inaccuracies arising from the high water content.[17] Although the authors stated that the experiments were repeated, kinetic effects might have played a role where the equilibrium loading was not fully reached. Although not explicitly reported in the literature, experiments currently ongoing in our group reveal a noticeable tailing in the CO_2 uptake curves, suggesting a remarkably prolonged equilibration period. A similar trend can be discerned upon close inspection of published uptake data.

2.3.2 Isotherm fitting. In this work, the co-adsorption isotherm was modeled using the weighted average dual site Toth (WADST) model first proposed by Young et al.[17] The model assumes the presence of two available types of adsorption sites: dry sites (without a water molecule) and wet sites (with an available water molecule). The probability that a site is occupied by water is described using an Arrhenius-like distribution, analogous to a Maxwell–Boltzmann exponential form,[17]

$$q_{\text{CO}_2}^{\text{co}} = \left(1 - e^{-\frac{A}{q_{\text{H}_2\text{O}}}}\right)q_{\text{dry}}(p, T) + e^{-\frac{A}{q_{\text{H}_2\text{O}}}}q_{\text{wet}}(p, T) \tag{4}$$

where q_{dry} refers to the Toth model fitted in Section 2.1.2, q_{wet} represents the Toth model to be fitted, accounting for the humid contribution of the model, and A refers to the probability distribution parameter.

The fitting results are reported in Fig. 4, where the model accurately captures the dependency of CO_2 loading on relative humidity. The fitted parameters are reported in Table 4.
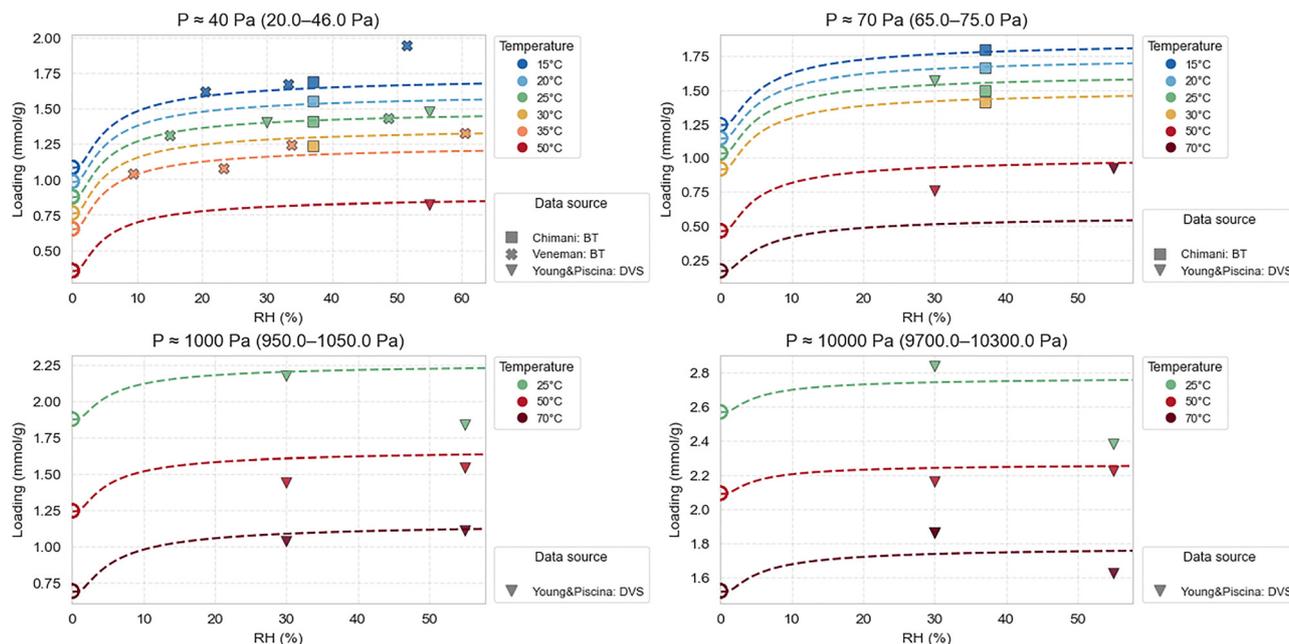
Fig. 4 Binary CO_2–H_2O isotherms collected from different authors and measurement techniques. DVS refers to dynamic vapor sorption, and BT to breakthrough experiments. Empty circles refer to the dry data point.

Table 4 Optimized parameters of the WADST model for binary CO_2–H_2O adsorption

Parameter	Value	Unit
$b_{0,wet}$	6780.19	—
$\Delta H_{0,wet}$	130 526.77	J mol^{-1}
$\tau_{0,wet}$	0.1480	—
α_{wet}	0.2012	—
$q_{m,wet}$	4.592	mmol g^{-1}
A_{fact}	0.2609	—
MAE	0.0881	mmol g^{-1}
RMSE	0.1201	mmol g^{-1}
R^2	0.9822	—

It is worth noting that several recent studies on DAC process modeling have relied on the empirical modified Toth model proposed by Stampi-Bombelli *et al.*, hereafter referred to as the SB model.[33–35] This model has often been adopted in the literature due to its simplicity and straightforward implementation. However, as shown in Fig. S7 (SI), the SB model provides a poorer fit to the cured co-adsorption dataset compared to the WADST model.

Beyond the isotherm fitting, a second and even more critical limitation emerges at the process level. As discussed in Section S1.6 (SI), in line with the observations of Young *et al.*,[17] the SB model predicts worse process performances than the dry case, opposite to the expected enhancement effect brought by humid air. This counterintuitive result originates from the fact that the SB formulation cannot properly describe CO_2 desorption: a significant fraction of CO_2 remains stored inside the adsorbent but is not released and collected, as shown in Fig. S6. Importantly, this is not only a qualitative inconsistency but also quantitatively relevant. In the full quantitative comparison

reported in the SI, the SB model leads to a higher equivalent work (4.08 → 4.91 MJ kg$_{CO_2}^{-1}$) and to substantially reduced productivity (38.6 → 31.5 kg$_{CO_2}$ per m^3 per day) and total yield (58.0% → 38.5%) compared to the dry case (Table S1). As a consequence, the SB model underestimates the cyclic working capacity and collected CO_2, while overestimating the internal CO_2 loading during desorption.

Mechanistically, this behavior arises from the way the SB model introduces the dependency of CO_2 loading on H_2O. Specifically, q_{CO_2} is coupled to q_{H_2O} through the parameters q_m and b. Since water adsorption is described by the GAB isotherm, q_{H_2O} is almost independent of temperature. Therefore, even at high temperatures where desorption should occur, the GAB isotherm still predicts high water loadings. Through the SB formulation, this translates into artificially high CO_2 loadings during desorption, despite the fact that CO_2 uptake should physically decrease. In practice, H_2O enhances the apparent CO_2 loading at desorption, leading to unrealistically high internal storage inside the adsorber and ultimately to degraded process performance.

For these reasons, the SB model may not be suitable for reliable process simulations under humid conditions. In contrast, the WADST model overcomes these limitations by providing a more consistent description of both adsorption and desorption behavior.

3 Detailed process modeling

In this work, we consider TVSA cycle design, which has become a benchmark for DAC in industry and scientific research.[11,17,20,33–38] TVSA is particularly suited for DAC because of the stringent purity requirements and the harsh desorption conditions.

Capturing ultra-diluted CO_2 from air demands strong adsorption, which inevitably increases the energy required during desorption. A combined application of heat and vacuum therefore represents an effective regeneration strategy. In addition, the inclusion of a blow-down step in TVSA enhances control over CO_2 purity, as it enables purging of residual inert gases from the bed.[39]

3.1 Process configurations

A visual representation of the process configuration employed in this work is shown in Fig. 5. Ambient air consisting of CO_2, H_2O, N_2 and O_2 flows through a jacketed packed-bed adsorber during the adsorption step (ADS). Then, during the blow-down step (BD), pressure in the column is brought to vacuum conditions using a vacuum pump at the outlet of the bed. This step will purge the majority of N_2 and O_2, controlling the purity of the product stream. A pre-heating step (PH) *via* wall heating is then required for two main reasons: (i) the gas displacement will enforce the evacuation of any leftover inert in the column, along with a portion of the adsorbed water and CO_2, ensuring a stricter control on product purity; (ii) for the cycle configuration where steam is employed, the temperature of the bed must be brought above the steam condensation temperature to avoid the presence of liquid water inside the adsorbent bed. Two modes of desorption (DES) will be considered: wall-heated (WH) and steam-assisted (SA). In the wall-heated configuration, heat will be delivered from the walls to the bed through the heating jacket only. However, the effectiveness of this approach might decrease when a bigger bed radius is considered, due to reduced heat transfer to the bulk *via* inefficient packed-bed conduction. Therefore, steam is employed to help the desorption

Table 5 Ambient operating conditions employed for the adsorption step

Parameter	Value
CO_2 mole fraction, y_{CO_2}	400 ppm
Relative humidity, RH	50%
Ambient temperature, T_{amb}	25 °C
Ambient pressure, p_{amb}	101 325 Pa
Mole fraction ratio,[40] y_{O_2}/y_{N_2}	20.94/78.08

phase not only by delivering latent heat of condensation directly to the bed but also by favoring evacuation due to fluid displacement. To enforce purity constraints, a condenser is placed downstream of the bed to remove most of the water from the product stream. This also reduces the load on the vacuum pump, which has to handle a smaller gas volume, thereby lowering the energy demand. Finally, pressure is brought back to ambient conditions during the pressurization step (PS), where fresh air is blown into the bed. The subsequent cycle can then start, with the new adsorption step used as an active cooling step to bring back the temperature to ambient conditions (Table 5).

3.2 Process simulation

3.2.1 Governing equations. The mathematical description of the process is based on the conservation balances of the individual species, the total mass, and the thermal energy of both the adsorbent bed and its wall boundary, giving rise to a system of eight PDEs.

The key assumptions of the model are listed below:
- The fluid behaves as an ideal gas;
- The flow is described by an axially dispersed plug-flow regime;
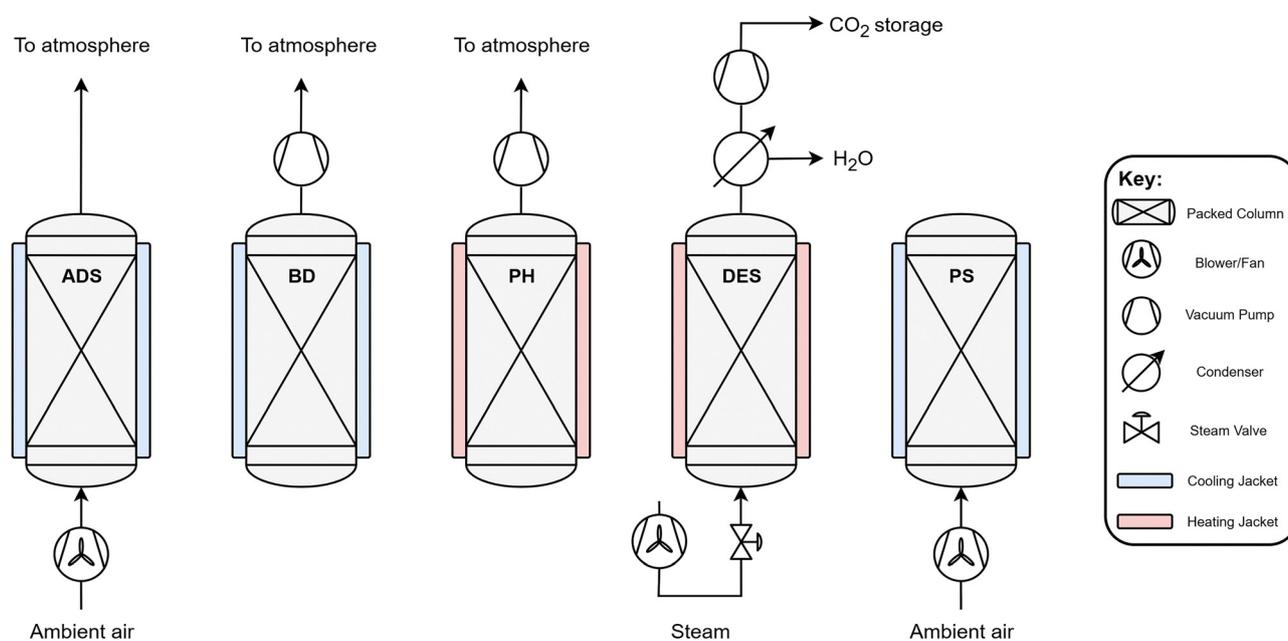- Gradients in the radial direction are neglected;

Fig. 5 TVSA cycle process scheme used in this work. Cycle steps follow the order reported: adsorption (ADS), blow-down (BD), pre-heating (PH), desorption (DES), and pressurization (PS). Depending on the steam valve position, the process can be operated in two modes: (i) steam-assisted-TVSA, where steam is used to help the desorption step, and (ii) wall-heated-TVSA, where only the heat jacket is used during desorption.

- N_2 and O_2 are considered as non-adsorbing species;[18]
- The densities, thermal conductivities, and axial gas dispersion coefficients are temperature-independent and constant throughout the reactor;
- Instantaneous thermal equilibrium is established between the fluid and the solid phase;
- The gas velocity field is obtained from a packed-bed pressure-drop closure (Kozeny–Carman relation), where the axial velocity is computed from the axial pressure gradient;
- The adsorption kinetics is described by the linear driving force approximation (LDF).[41–43]

The resulting full set of non-dimensional governing equations is given below:

$$\frac{\partial y_i}{\partial \tau} + y_i \left(\frac{1}{\bar{p}} \frac{\partial \bar{p}}{\partial \tau} - \frac{1}{\bar{T}} \frac{\partial \bar{T}}{\partial \tau} \right) = -\frac{\bar{T}}{\bar{p}} \nabla \cdot \left(\frac{\bar{p}}{\bar{T}} y_i \vec{v} \right)$$
$$-\frac{\bar{T}}{\bar{p}} \nabla \cdot \left(-\frac{1}{Pe_m} \nabla \frac{\bar{p}}{\bar{T}} y_i \right) \quad (5)$$
$$-\frac{\bar{T}}{\bar{p}} \psi_{ads,i} \frac{\partial x_i}{\partial \tau}$$

$$\frac{\partial x_i}{\partial \tau} = \alpha_i (x_i^* - x_i) \quad (6)$$

$$\frac{\partial \bar{p}}{\partial \tau} - \frac{\bar{p}}{\bar{T}} \frac{\partial \bar{T}}{\partial \tau} = -\bar{T} \nabla \cdot \left(\frac{\bar{p}}{\bar{T}} \vec{v} \right) - \bar{T} \sum_{i=1}^{n_{comp}} \nabla \cdot \left(-\frac{1}{Pe_m} \nabla \frac{\bar{p}}{\bar{T}} y_i \right)$$
$$- \bar{T} \sum_{i=1}^{n_{comp}} \psi_{ads,i} \frac{\partial x_i}{\partial \tau} \quad (7)$$

$$\frac{\partial \bar{T}}{\partial \tau} - \Omega_p \frac{\partial \bar{p}}{\partial \tau} = -\Omega_c \bar{c}_{tot} \vec{v} \cdot \nabla \bar{T} + \Omega_k \nabla^2 \bar{T} - \sum_{i=1}^{n_{comp}} \psi_{heat,i} \frac{\partial x_i}{\partial \tau}$$
$$+ \Omega_w (\bar{T}_w - \bar{T}) \quad (8)$$

$$\frac{\partial \bar{T}_w}{\partial \tau} = \Omega_{kw} \nabla^2 \bar{T}_w - \Omega_w^{int} (\bar{T}_w - \bar{T}) + \Omega_w^{ext} (\bar{T}_j - \bar{T}_w) \quad (9)$$

Here, the overbar indicates non-dimensional variables obtained using the reference values defined in Section S2.1 of the SI, which also provides the definitions and descriptions of all parameters used in the system.

3.2.2 Closure models. Additional constitutive relations are required for the description of momentum, mass, and heat transfer. These semi-empirical expressions, commonly referred to as closure models, provide correlations for parameters such as the pressure drop, axial dispersion coefficient, and heat transfer coefficients. More information about the adopted equations can be found in the SI. It is worth noting that, while LDF kinetic coefficients are mechanistically expected to exhibit the temperature dependence, quantitative correlations for DAC-relevant solid amines under co-adsorption conditions remain material- and regime-specific and are still an active research topic. Recent studies (including work from our group) have started to quantify temperature-dependent kinetics for DAC sorbents.[44,45] In the present study, we therefore adopt

temperature-invariant LDF coefficients as a simplifying assumption to limit parametric uncertainty and enable consistent comparisons across configurations; incorporating validated temperature-dependent kinetics will be addressed in future work.

Particular attention is given to radial heat transfer from the heated wall to the packed-bed bulk, which governs regeneration in the wall-heated configuration, where wall to bed heat transfer becomes rate limiting as the bed radius increases. Rather than using a constant internal heat transfer coefficient, we adopted an overall 1D internal heat transfer coefficient U_w, following the 2D → 1D reduction developed by Dixon *et al.*, as shown in eqn (10),[46–48]

$$U_w = \left(\frac{1}{h_w} + \frac{d_b}{6\lambda_{rad}} \frac{Bi + 3}{Bi + 4} \right)^{-1} \quad (10)$$

where h_w is the internal convective heat transfer coefficient, λ_{rad} is the effective radial conduction, Bi is the Biot number and d_b is the bed internal diameter. This enhanced formula allows us to better capture the shifting balance between wall convection (h_w) and radial conduction (λ_{rad}) as a function of the bed radius. The complete sets of definitions and equations required for the heat transfer model are reported in the SI.

Following the approach of Ward *et al.*, the downstream condenser and vacuum pump were modeled as two equilibrium separator stages in series, with O_2 and N_2 being incondensable species. In their study, the optimal configuration was empirically identified as having the condenser upstream of the vacuum pump, with the condenser removing most of the H_2O and the pump providing a final knockout upon discharge. In addition to this separation-driven rationale, we highlight that positioning the condenser before the vacuum pump also yields a substantial energy advantage: by condensing water vapor prior to evacuation, the gas load handled by the pump is drastically reduced, thereby lowering its energy consumption.

3.2.3 Numerical implementation. The system of PDEs described above, together with all the additional equations, was solved numerically using an in-house finite-difference solver based on the method of lines (MOL), implemented in Python 3.12.2. The PDEs were first semi-discretized in the spatial dimension and transformed into a set of ordinary differential equations (ODEs) *via* finite-difference schemes using the pymrm package developed in our group.[49] Then, the resulting ODE system was integrated with the open-source SUNDIALS library (SUite of nonlinear and DIfferential/ALgebraic equation solvers), using the CVODE module.[50,51] The solver was accessed using the Python interface provided by scikit-SUNDAE.[52] CVODE was used in stiff mode with the backward differentiation formula (BDF), and convergence was controlled with relative and absolute tolerances of 10^{-6} and 10^{-8}, respectively. To ensure numerical robustness in the presence of the ppm-level O_2 and CO_2, the governing equations were implemented in a non-dimensional and normalized formulation, such that each state variable is scaled to the $[0,1]$ interval. This improves conditioning and mitigates stiffness

that typically arises when simultaneously resolving major species and ppm-level components. Finally, it is worth noting that the oxygen specification is enforced on the integrated product stream composition rather than on local point-wise concentrations, which reduces sensitivity to local numerical noise.

Each step of the TVSA cycles was simulated using its own set of boundary conditions, while the initial conditions were taken from the previous simulated step. The full cycle is solved by simulating each step sequentially until the cyclic-steady-state (CSS) is reached. The CSS was defined as the condition in which the relative difference between all eight simulated outlet profiles after the pressurization step and those of the previous cycle was within 0.5%.

The model was validated against cyclic-steady-state (CSS) outlet profiles reported by Young *et al.* (Fig. S9–S11 in the SI), showing excellent agreement. In addition, an independent validation was performed against experimental dynamic breakthrough data for Lewatit® VPOC 1065, as reported by Petersen *et al.* (Fig. S12 in the SI), confirming that the present column model captures the dominant transient uptake dynamics under different DAC-relevant conditions. Interestingly, the LDF mass-transfer coefficient fitted from the Petersen dataset ($k_{LDF} \approx 2 \times 10^{-3}$ s^{-1}) is close to the value adopted in the main text based on the study by Young *et al.* ($k_{LDF} \approx 3 \times 10^{-3}$ s^{-1}), despite the substantially different column geometries and operating conditions. This consistency supports the transferability of the kinetic parameter order of magnitude across different experimental configurations and indicates that the model is not overly dependent on case-specific parameter tuning. Full details on boundary conditions, validation cases, and numerical solver settings are provided in the SI.

3.3 Optimization framework

3.3.1 Key performance indicators. To assess the performance and feasibility of the purity-constrained DAC process, the trade-off between the energy input and the actual CO$_2$ captured is investigated. For the latter, the productivity KPI (kg_{CO_2} m^{-3} d^{-1}) was defined:

$$\Pi_{CO_2} = \frac{m_{CO_2}^{des}}{V_{bed} t_{cycle}} \quad (11)$$

where $m_{CO_2}^{des}$ refers to the CO$_2$ mass obtained in the desorption step after the condenser and the vacuum pump discharge, V_{bed} is the adsorber bed volume and t_{cycle} refers to the total cycle time in the CSS. The energy contributions are divided into electrical and thermal contributions. For each step, we defined the specific electrical contribution as the combination of (i) compression energy and (ii) vacuum pump energy. Therefore, the total electrical energy consumption (MJ $kg_{CO_2}^{-1}$) is calculated as follows:

$$E_{el} = \sum_{i=1}^{N_{steps}} \frac{e_{comp,i} + e_{vac,i}}{m_{CO_2}^{des}} \quad (12)$$

The thermal energy requirement is partitioned into (i) heating the jacket, (ii) steam generation, and (iii) water condensation

in the downstream condenser. Unlike previous studies, we explicitly model the condenser and include its heat-removal duty in the energy use. This captures the non-negligible load associated with condensing co-desorbed H$_2$O, providing a more realistic estimate of plant-level energy consumption (MJ $kg_{CO_2}^{-1}$):

$$Q_{th}^{hot} = \sum_{i=1}^{N_{steps}} \frac{q_{jack,i} + q_{steam}}{m_{CO_2}^{des}}, \quad Q_{th}^{cold} = \frac{q_{cond}}{m_{CO_2}^{des}} \quad (13)$$

To obtain a unique representative metric of the process energy requirement, we therefore expressed all thermal duties in terms of equivalent work. While electrical and thermal contributions can be evaluated separately, a direct summation would be misleading because the two energy forms have different qualities. In particular, thermal energy cannot be fully converted into work, as limited by the second law of thermodynamics. Following the approach of Danaci *et al.*, the hot-side thermal inputs were weighted by the Carnot efficiency and corrected with a turbine effectiveness, while the cold-side condenser duty was converted into an equivalent electrical demand through a COP-based refrigeration model:[53]

$$W_{eq} = E_{el} + \eta_{turb}\left(1 - \frac{T_L}{T_H}\right)Q_{th}^{hot} + \eta_{refr}\left(\frac{T_{cond}}{T_L - T_{cond}}\right)Q_{th}^{cold} \quad (14)$$

where the terms T_H and T_L represent the desorption and ambient temperatures, respectively, while T_{cond} denotes the condenser operating temperature. A turbine effectiveness of $\eta_{turb} = 0.75$ and a refrigeration effectiveness of $\eta_{refr} = 0.5$ were selected to remain consistent with commonly adopted DAC-TVSA benchmarking practice. Using alternative values from the literature would mostly translate the absolute W_{eq} axis but would not alter the relative ranking and qualitative conclusions. The evaluation of each individual energy term can be found in the SI.

Finally, the purity of the product stream after the vacuum discharge was evaluated. As a reference target, we adopted the specifications of the ARAMIS project in the Netherlands, which aims to develop the infrastructure for CO$_2$ transport and storage.[54,55] The provided specifications led to the definition of two purities KPIs: (i) CO$_2$-based purity (>95 mol%) and (ii) O$_2$-based content (<40 ppm mol).

$$Pu_{CO_2} = \frac{m_{CO_2}^{des}}{\sum_i m_i^{des}} \quad (15)$$

$$\phi_{O_2} = \frac{n_{O_2}^{des}}{\sum_i n_i^{des}} \quad (16)$$

where the i index refers to CO$_2$, H$_2$O, O$_2$ and N$_2$ species.

3.3.2 Multi-objective optimization. Process performance in TVSA is governed by the choice of operating conditions at the cycle level, from step durations to feed velocities, *etc.* To explore how operating conditions affect capture, energy use, and product composition, we optimized the cycle timings, setpoints,

and inlet velocities within physically and operatively meaningful bounds. Let the decision vector collect these variables as

$$\mathbf{x} = [t_{\mathrm{ads}}, t_{\mathrm{heat}}, t_{\mathrm{des}}, T_{\mathrm{des}}, p_{\mathrm{vac}}, v_{\mathrm{feed}}, v_{\mathrm{steam}}]^{\mathrm{T}} \in \mathbb{R}^7,$$

where t_{ads} is the adsorption step duration, t_{heat} is the wall-heating (preheating) duration, t_{des} is the desorption step duration, T_{des} is the desorption temperature setpoint, p_{vac} is the absolute bed pressure targeted during the vacuum step, v_{feed} is the superficial velocity of the air feed during adsorption and v_{steam} is the superficial velocity of the regeneration steam during steam-assisted desorption (set to zero when steam is not used).

The bi-objective-constrained problem is then defined as follows:

$$\min_{\mathbf{x}\in\Omega} \quad \mathbf{f}(\mathbf{x}) = \begin{bmatrix} f_1(\mathbf{x}) \\ f_2(\mathbf{x}) \end{bmatrix} = \begin{bmatrix} -\Pi_{\mathrm{CO_2}}(\mathbf{x}) \\ W_{\mathrm{eq}}(\mathbf{x}) \end{bmatrix}, \tag{17}$$

$$\text{s.t.} \quad g_1(\mathbf{x}) = 0.95 - \mathrm{Pu}_{\mathrm{CO_2}}(\mathbf{x}) \le 0, \tag{18}$$

$$g_2(\mathbf{x}) = \phi_{\mathrm{O_2}}(\mathbf{x}) - 40 \times 10^{-6} \le 0, \tag{19}$$

$$g_3(\mathbf{x}) = T_{\mathrm{cond}}^{\mathrm{steam}}(\mathbf{x}) - T_{\mathrm{out}}^{\mathrm{ph}}(\mathbf{x}) \le 0, \tag{20}$$

$$\ell_i \le x_i \le u_i, \quad i = 1, \ldots, 7 \tag{21}$$

with $\Omega = \{\mathbf{x} \in \mathbb{R}^7 : \ell \le \mathbf{x} \le u\}$, where ℓ and u represent the lower and upper bounds (see Table 6). Note that eqn (20) was added to force the bed temperature (T_{out}) to be always greater than the steam condensation temperature ($T_{\mathrm{cond}}^{\mathrm{steam}}$), at the given vacuum pressure value.

Given the multi-objective nature of the problem, and the expensive objective function evaluation, we solved (17)–(21) using the constrained non-dominated sorting genetic algorithm (NSGA-II), implemented in Python via the pymoo optimization framework.[56,57]

Each optimization run employed a population size of 250 over 250 generations. The genetic operators were configured with simulated binary crossover (SBX) with a crossover probability of $p_c = 0.9$ and a distribution index of $\eta_c = 15$, together with polynomial mutation $\eta_m = 20$.[58] Duplicate solutions were eliminated at each generation to maintain population diversity, while the initial population was sampled using the latin hypercube sampling method.

Table 6 Bounds for the decision variables used in the MOO formulation

Variable	Symbol	Bounds	Unit
Adsorption time	t_{ads}	1800–36 000	s
Heating time	t_{heat}	300–36 000	s
Desorption time	t_{des}	300–36 000	s
Desorption temperature	T_{des}	363.15–373.15	K
Vacuum pressure	p_{vac}	0.05–0.5	Bar
Feed velocity	v_{feed}	0.001–1	m s^{-1}
Steam velocity^a	v_{steam}	0.001–1	m s^{-1}

^{a} Only active for steam-assisted desorption.

4 Process modeling results

Unless explicitly specified, all the parameters used for the process modeling are reported in the reference parameter set available in Section S2.5 of the SI.

4.1 Literature benchmark

An overview of the optimization results is presented in Fig. 6, where the obtained Pareto fronts were first benchmarked against literature data on TVSA cycle optimizations for DAC. From the study by Balasubramaniam et al., four amine-functionalized sorbents were considered: TRI-PE-MCM-41 (TMCM-41), SI-AEATPMS (TPMS), APDES-NFC-FD-S (APDES), and NbOFFIVE-1-Ni (NbOFFIVE).[35] From the study by Ward et al., both the APDES Pareto front and the estimated operative region of Climeworks were included.[34]

In Fig. 6a, both wall-heated and steam-assisted configurations are compared against literature steam-heated cases. Notably, the APDES values from the study by Ward et al. appear significantly lower than the corresponding APDES values from the study by Balasubramaniam, even though both studies employed the same LDF kinetic constant. This discrepancy may arise from differences in the adsorber aspect ratio (bed height to diameter, 1/16 in the study by Ward versus 1/4 in the study by Balasubramaniam) or from slight variations in the isotherm model parameters adopted.

Two main details emerge from Fig. 6a. (i) At the reference aspect ratio ($H_{\mathrm{bed}}/D_{\mathrm{bed}} = 1/16$), the wall-heated configuration exhibits an extremely narrow productivity window. This constraint arises from the thermal bottleneck imposed by wall-to-bed heat transfer, which limits the system's ability to supply heat efficiently and leads to a steep rise in equivalent work as productivity increases. (ii) In the steam-assisted configuration, the feasible productivity range expands significantly, at the cost of additional steam generation and condensation duty. This performance gap originates in the desorption step, where in the wall-heated configuration, desorption remains bottlenecked by slow radial heat transfer, whereas in the steam-assisted configuration, the injection of steam removes this limitation by delivering heat volumetrically through condensation while simultaneously purging CO_2. This is confirmed by examining the optimized decision variable boxplots, shown in Fig. S13 and S14 in the SI. In the wall-heated case, the desorption time t_{des} consistently saturates at its upper bound, indicating that the maximum allowed desorption duration is required to overcome the radial heat transfer limitation. In contrast, in the steam-assisted case, the distribution of t_{des} collapses near the lower bound (around 5% of the normalized range), confirming that steam injection enables significantly faster desorption.

Remarkably, despite the additional energy term for the condenser and the stricter O_2-based purity constraint, the optimizer finds sets of operational parameters (steam flow, T_{des}, and vacuum depth) such that the Pareto front results are within literature ranges. Part of this robustness is also material-driven: the Lewatit sorbent exhibits high working capacity at
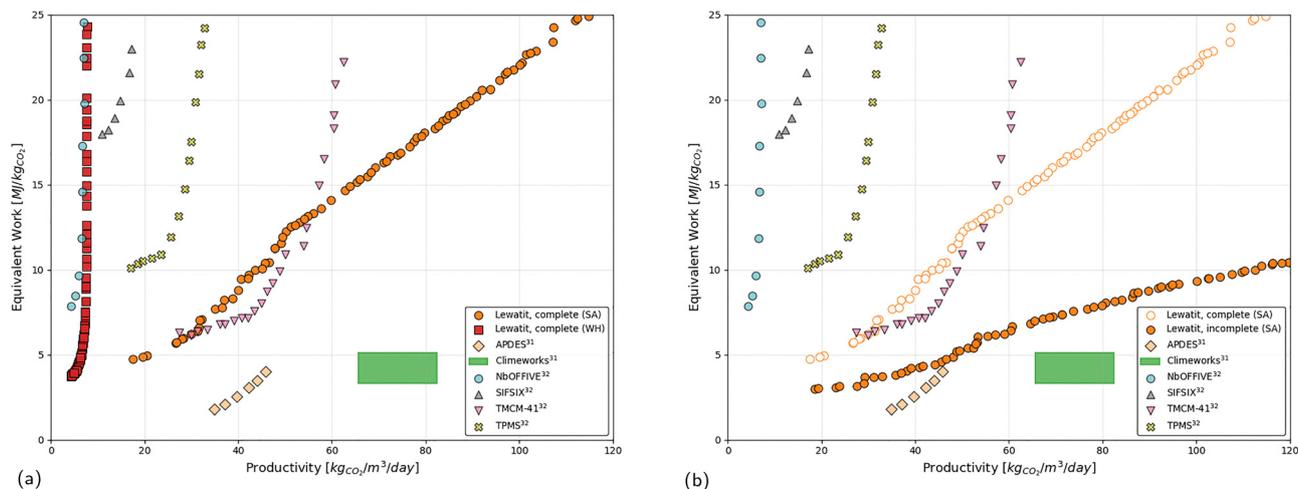
Fig. 6 Pareto front analysis. (a) Comparison of wall-heated and steam-assisted configurations with literature data. (b) Effect of including (complete) and excluding (incomplete) condenser duty and O_2 content constraint on the steam-assisted configuration, benchmarked against literature data.

DAC partial pressures with favorable kinetics, which helps maintain competitive W_{eq} at a given productivity.

The material-driven advantage is further highlighted in Fig. 6b, which shows results obtained without accounting for the condenser energy penalty and O_2 content constraint (incomplete case), thereby allowing a more direct comparison with literature data. The isolated impact of enforcing the O_2 specification alone is reported separately in the SI (Fig. S16). The Lewatit Pareto fronts display a significantly more favorable energy–productivity trade-off, approaching the values predicted by Ward *et al.* and the Climeworks operational range. This reflects both the higher intrinsic working capacity of Lewatit at DAC-relevant partial pressures and its ability to sustain competitive performance despite additional process constraints.

The remarkable difference between the incomplete and complete cases in Fig. 6b can be rationalized by analyzing the decision variable distributions shown in the SI. Comparing the boxplots of the (SA) complete case (Fig. S14) with those of the (SA) incomplete case (Fig. S15) shows that the largest shifts occur in the pre-heating duration and the steam velocity, which drive the observed performance difference. In the incomplete case, significantly higher steam velocities are allowed, with a broader distribution, since no energetic penalty is associated with the condenser. This allows more aggressive steam use, leading to deeper regeneration and, consequently, higher productivities. Conversely, in the complete case, the steam velocity distribution is much narrower, as larger steam flows directly translate into higher condenser duties. A similar trend is observed for the pre-heating time: in the incomplete case, it remains relatively short, as the sole requirement is to heat the bed above the steam condensation temperature to avoid liquid water formation. In contrast, when the O_2 specification is enforced, much longer pre-heating times are required to purge residual N_2 and O_2, resulting in longer cycles and reduced productivities.

These shifts in decision variable distributions also explain the progressively larger discrepancy between the complete and incomplete Pareto fronts. At low productivities, the impact of longer pre-heating and restricted steam flow is relatively modest, so the two formulations remain relatively close. However, as productivity increases, the penalties associated with both variables accumulate: the need for longer pre-heating increasingly reduces the productivity, while the restriction on steam use limits the extent of regeneration and adds condenser costs. Consequently, the energy gap between the complete and incomplete cases widens with productivity, ultimately leading to nearly a two-fold difference at the upper end of the Pareto front.

4.2 Aspect ratio

In the previous section, the bed aspect ratio emerged as a critical design parameter. At the reference value (H_{bed}/D_{bed} = 1/16), the bed is relatively flat, with a large diameter compared to its height. This geometry accentuates radial heat-transfer limitations, which become particularly severe during the pre-heating step (for both wall-heated and steam-assisted configurations) and the desorption step (for wall-heated operation). In both cases, the poor radial heat transfer imposed serious challenges in meeting the O_2 specification, requiring prolonged purging times regardless of whether steam was employed. While steam injection can partly overcome heat-transfer limitations during desorption, the pre-heating step remains inherently inefficient due to the large radial distance. Increasing the aspect ratio reduces the radial dimension and produces a more slender cylindrical geometry, thereby alleviating this bottleneck. To evaluate whether wall-heated configurations can regain competitiveness through aspect-ratio optimization and to benchmark this against steam-assisted operation, a dedicated parametric study was performed. The aspect ratios investigated, along with the corresponding bed heights and diameters, are summarized in Table 7.

4.2.1 Wall-heated configuration. As shown in Fig. 7a, as the aspect ratio increases, the wall-heated configuration exhibits clear performance trends. In line with the observations of Ward *et al.*, a shallow minimum in equivalent work is observed

Table 7 Geometry of the adsorber for different aspect ratios $\tau = H_{bed}/D_{bed}$. The bed volume is kept constant at 1.20×10^{-3} m^3 (ref. 34)

τ	Diameter (m)	Height (m)
1/16	0.290	0.018
1/8	0.230	0.029
1/4	0.183	0.046
1/2	0.145	0.072
1	0.115	0.115
4	0.072	0.290

for $\tau = 1/8$–$1/2$, although the effect is not dramatic. The impact of τ can be summarized in two main effects: (i) an expansion of the productivity span and (ii) a reduction in equivalent work. This decrease continues up to $\tau = 1$, while further increasing the aspect ratio (e.g., $\tau = 4$) leads again to higher energy requirements.

Beyond these general trends, an interesting observation is that the Pareto points are not uniformly distributed but tend to cluster around specific regions. This behavior is illustrated in Fig. 8a, which depicts the distributions of productivity and equivalent work within the Pareto front space using violin plots. In this representation, the width of each "violin" corresponds to the density of Pareto-optimal solutions: a pronounced bulge therefore indicates a higher concentration of solutions in that region of the trade-off. The red diamonds mark the marginal modes, i.e. the most probable values along each individual axis (productivity or work), while the yellow stars denote the joint modes, identifying the most statistically favored operating regimes when both objectives are considered simultaneously. A clear trend emerges: as highlighted previously, equivalent work exhibits a minimum around $\tau = 1/4$, while productivity steadily increases up to $\tau = 1$, after which it plateaus. Fig. 8b further illustrates this by reporting the extracted joint modes as a function of τ. These results show that the choice of the optimal aspect ratio depends on the design objective. If, for example, a maximum threshold of

$W_{eq} = 10$ MJ kg$_{CO_2}^{-1}$ is imposed while aiming to maximize productivity, then $\tau = 1$ is the most favorable geometry. Conversely, if the priority is to minimize equivalent work regardless of productivity, then $\tau = 1/4$ represents the optimal configuration.

A further analysis of the operational variable distributions explains the observed behaviors. In Section S4.1 of the SI, we report the distributions of the optimized step durations again via violin plots. Similar to the clustering patterns shown in Fig. 8a and b, the violin plots of the step durations also display distinct clusters, with the marginal modes highlighted in red, emphasizing the underlying statistical trends. As shown in Fig. S17, the adsorption time increases with the aspect ratio, since flatter geometries allow for faster adsorption (the gas interacts with more solid per unit bed length), while larger τ values require longer times for the bed to saturate for the opposite reason. However, Fig. S18 and S19 show that both the pre-heating time and the desorption time decrease with increasing τ, due to the more favorable area-to-volume ratio that enhances radial heat transfer. Overall, the combined effect results in a net reduction of the total cycle time, as reported in Fig. S20. Shorter cycles enable higher productivities, as less time is lost during purging and fewer CO$_2$ losses occur.

On the other hand, the longer adsorption time required to fill the bed affects the equivalent work in two ways: (i) higher compression energy due to the prolonged adsorption step and (ii) higher compression energy associated with the increased pressure drop. This behavior is confirmed by inspecting Fig. S21–S24, which show the violin plots of the energy term distributions. As shown, increasing τ leads to higher compression work, while the contributions from pre-heating, desorption, and condenser duties (which account for the majority of the equivalent work) decrease. The net result is the emergence of a minimum in equivalent work, which directly reflects the trade-off between pressure drop and heat-transfer efficiency in packed-bed systems. From a design standpoint, this result implies that the aspect ratio should not be selected solely to maximize
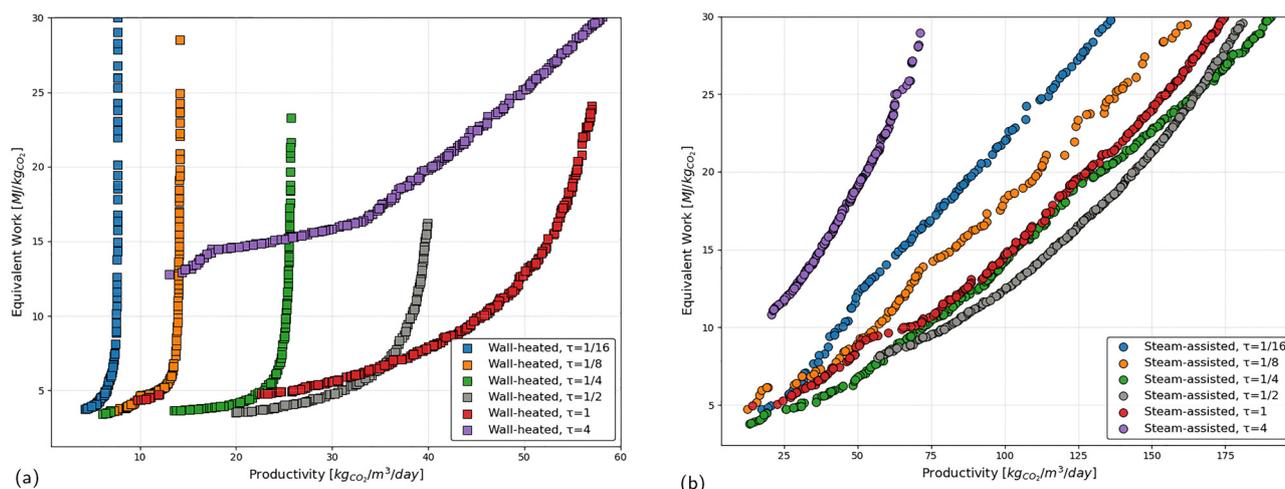

Fig. 7 Effect of the aspect ratio ($\tau = H_{bed}/D_{bed}$) on the Pareto fronts of DAC adsorbers. (a) Wall-heated configuration for different τ values. (b) Steam-assisted configuration for different τ values.
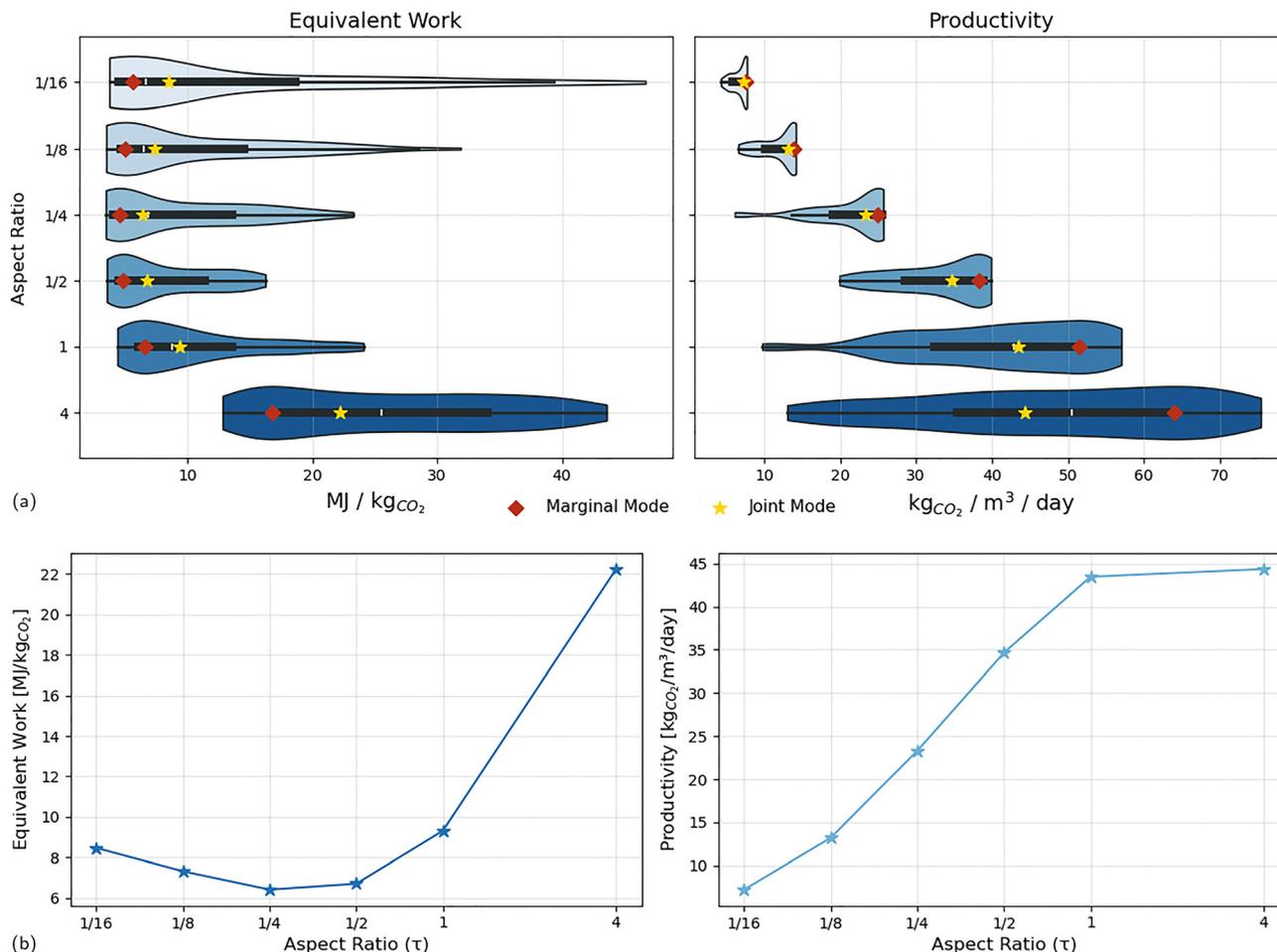
Fig. 8 Clustering of Pareto-optimal solutions in the wall-heated configuration. (a) Violin plots of productivity distributions for different aspect ratios, with modes highlighted. (b) Joint modes of productivity and equivalent work as a function of aspect ratio, showing the emergence of preferential operating regimes.

productivity or solely to reduce thermal duties. The existence of a shallow minimum therefore indicates that intermediate geometries provide the most balanced compromise, whereas extreme aspect ratios are dominated by a single limiting mechanism (heat-transfer limitation at low τ and hydraulic limitation at high τ).

4.2.2 Steam-assisted configuration. As shown in Fig. 7b, both productivity and energy cost domains are substantially expanded compared to the wall-heated case, a direct consequence of steam injection, reaching productivity values as high as 180 kg_{CO_2} m^{-3} day^{-1} while keeping the equivalent work within 30 MJ $kg_{CO_2}^{-1}$. As previously mentioned, by providing heat volumetrically through condensation, steam enables rapid and complete desorption, which not only shortens the required desorption time but also increases the amount of CO_2 released per cycle. This combination allows the process to reach much higher productivities at a given energy cost, offering a degree of flexibility that is unattainable with wall heating.

If we now focus on how the ranges vary with the bed aspect ratio τ, the steam-assisted configuration does not show the progressive expansion of the productivity window observed in

the wall-heated case. Instead, for almost every τ, the productivity range already spans nearly the full extent of the plot (with the exception of $\tau = 1/2$ and $\tau = 4$). This is even more pronounced for the equivalent work, where the feasible range nearly covers the entire vertical axis of the plot for all aspect ratios, indicating that the steam-assisted configuration can access the full spectrum of energy costs regardless of τ. The only exception is $\tau = 4$, which behaves as an outlier. In other words, the intrinsic flexibility of the steam-assisted system delivers wide operative windows across all aspect ratios.

Unlike the wall-heated case, the distribution of Pareto-optimal solutions is not clustered around a single point but rather appears more homogeneously spread across the productivity–work space. As a result, marginal and joint mode analyses cannot be meaningfully applied in this case to study the observed trade-off given by the geometry. This behavior is illustrated in Fig. S25 of the SI, where the violin plots appear more smeared out instead of bulging around one dominant value, reflecting a more uniform density of solutions. The absence of strong clustering highlights that, once the radial heat-transfer bottleneck is removed by steam injection, the

performance becomes governed by a wider set of variable combinations, leading to a smoother energy–productivity landscape across geometries.

Given these circumstances, namely, the homogeneous distribution of solutions and the wide operative windows, the identification of optimal trends becomes more straightforward than in the wall-heated configuration. From a visual inspection of Fig. 7b, the most favorable trade-off between productivity and equivalent work is achieved at $\tau = 1/2$. This optimal region can be explained by analyzing the cycle step durations (see Fig. S26), where a minimum in total cycle time is observed. This minimum arises from a trade-off between the increased adsorption time and reduced the pre-heating time, as discussed previously for the wall-heated configuration. A modest minimum is also observed for the desorption time, further contributing to the productivity maximum.

4.2.3 Configuration envelopes and discussion. In summary, both configurations revealed the existence of an optimal bed aspect ratio range under the present modeling assumptions, arising from a trade-off between efficient heat transfer (most strongly impacting the pre-heating step) and the penalties associated with pressure drops. In the wall-heated case, this balance defines a narrow operative window and limits desorption performance. In contrast, steam injection fundamentally alters the picture, removing the bottleneck during desorption and effectively unlocking a new region of operation. To better visualize the impact brought by enhancing the desorption step, we computed the minimum-work envelopes for each mode (wall-heated, steam-assisted) as a function of productivity. For each mode and each productivity, we extracted the minimum of equivalent work, defining a discrete lower envelope. The two envelopes were then plotted together, as shown in Fig. 9.

Fig. 9a shows the global Pareto envelopes for wall-heated and steam-assisted configurations, illustrating how steam unlocks the extended operating region mostly by alleviating the desorption bottleneck. A clearer breakdown of these

advantages is presented in Fig. 9b. The red-shaded area identifies the energy premium region, where steam requires more equivalent work than wall heating at the same productivity. Conversely, the green-shaded area marks the energy savings region, where steam injection reduces the equivalent work compared to wall heating. Finally, the light-blue shaded area indicates the newly accessible operating region, where only steam-assisted operation can reach, thereby expanding the productivity frontier beyond the limits imposed by wall heating alone.

These findings underscore several key aspects. From our DAC-TVSA cycle simulations, the most critical energy contributions arise from three sources: (i) the pressure drop across the bed, (ii) the pre-heating energy required to purge nitrogen and oxygen and to exceed the steam condensation temperature, and (iii) the energy delivered during desorption, which must be both rapid and cost-effective. With the aim of tackling the first point and second point, our geometry study showed that these bottlenecks can be mitigated by tailoring the adsorber design, with an optimal region emerging between extremely flat beds and conventional elongated packed beds. The development of tailored geometries is essential for enabling large-scale DAC deployment. Ideally, a DAC unit should combine three features: (i) high sorbent loading, to maximize the amount of CO_2 captured; (ii) large gas–bed contact areas, to ensure rapid saturation and thus shorter cycle times; and (iii) low pressure drops, to minimize the energy penalty for gas transport. Geometry and heat transfer are inherently coupled when indirect heating is applied, as in the case of wall-heated configurations. Enhancing heat delivery to the bed would not only improve purging efficiency during pre-heating but could also provide a practical alternative to steam in the desorption step. In fact, while steam injection has proven to be highly effective for achieving rapid and efficient desorption, it poses significant challenges in terms of both energy consumption and technological implementation. While commercial level productivity
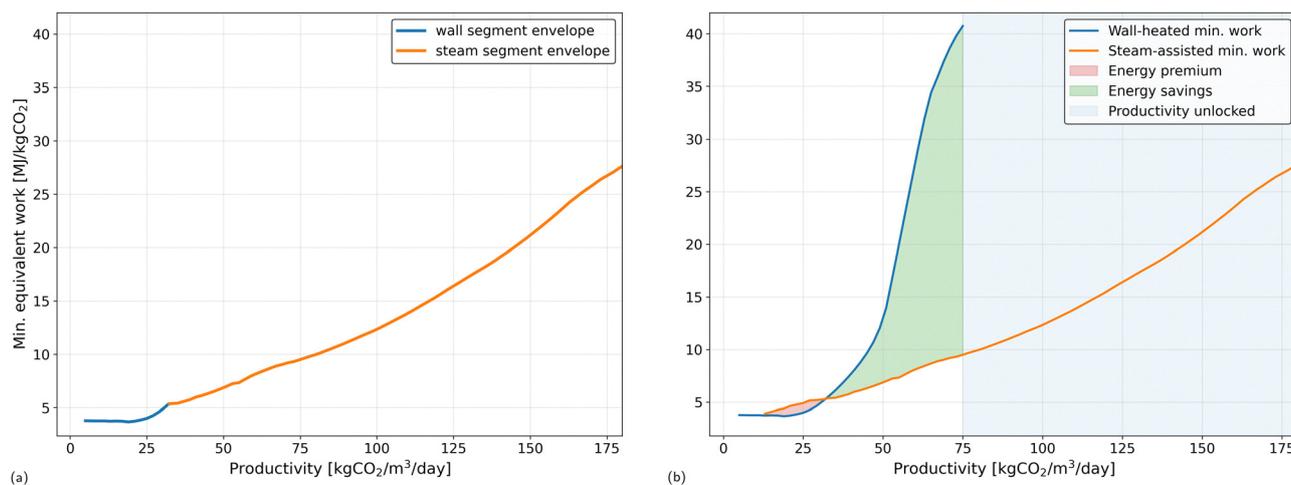

Fig. 9 Minimum work envelopes as a function of productivity for wall-heated and steam-assisted configurations. (a) Global Pareto envelopes highlighting the active mode at different productivity levels. (b) Mode comparison showing the regions of energy premium (red), energy savings (green), and the new accessible operating window unlocked by steam-assisted desorption (light blue).

regions were achieved, the associated energy cost was prohibitively high, particularly when compared to the estimated operating range of Climeworks. This underlines the need to pursue alternative heating strategies that are more economical yet as effective as steam assisted requirement, to exploit the new productivity region while reducing the current cost.

Conclusions and remarks

A comprehensive TVSA modeling framework was developed to provide a more accurate representation of DAC-TVSA performance, focusing on both wall-heated and steam-assisted design configurations. The study was carried out using Lewatit VPOC 1065, a benchmark amine-functionalized sorbent widely adopted in DAC research and industrial practice for its high CO_2 capture capacity and its commercial availability. We offered a critical assessment of literature benchmarks and introduced visualization tools to highlight trade-offs and optimization opportunities, ultimately pointing to strategies that could help close the gap toward commercial DAC deployment.

First, the thermodynamics description was enhanced for both unary and binary CO_2–H_2O isotherms. New datasets were created by collecting all the available data in the literature, followed by a data curation analysis where consistency between sources was prioritized. The co-adsorption aspect, both yet not fully understood and often oversimplified in the literature, was tackled by using the WADST isotherm model on the newly generated co-adsorption dataset. The WADST model was superior with respect to the widely used Stampi-Bombelli model, which posed serious issues when used in cyclic adsorption process simulations, due to inabilities to accurately describe the desorption step, along with an inferior descriptive performance.

The TVSA process model was developed with a particular focus on accurately capturing aspects often oversimplified in recent literature, such as radial heat transfer and the integration of downstream process equipment. On top of this detailed framework, a multi-objective optimization strategy was implemented to quantify the typical energy–productivity trade-offs of DAC-TVSA cycles. A key novelty of this work is the explicit enforcement of oxygen content constraints on the optimized solutions, in line with commercial CO_2 transport specifications, an aspect not previously addressed in the DAC modeling literature.

The obtained optimized solutions were first benchmarked against literature data, demonstrating that despite enforcing stricter process constraints, optimized solutions remain comparable with previously reported ranges. This underlined the robustness of the Lewatit sorbent and the optimization framework. More importantly, results emphasized that neglecting such constraints can lead to overly optimistic performance estimates, reaching an equivalent work overestimation of nearly 50% in the productivity ranges commercially covered.

The modeling effort allowed us to highlight the bottlenecks of the two considered configurations. The wall-heated design failed in reaching competitive productivity ranges, unlocked when using steam to drive the desorption step, at the cost of higher energy expenditure. However, the study revealed that both design strategies were severely hindered by the efficiency of the pre-heating step, which in our framework plays a critical role in enforcing the O_2 content specification, emerging as a major contributor to the overall process performance. In both configurations, this step is significantly limited by the wall-to-bed heat transfer resistance, ultimately becoming a dominant bottleneck that strongly influences the attainable productivity and equivalent work.

The impact of the aforementioned bottlenecks in both configurations was further investigated by enhancing the indirect wall heating through systematic variation of the adsorber aspect ratio. Reducing the radial dimension increased the available heat transfer surface area per unit volume, thereby relaxing radial heat transfer resistances. The analysis revealed the existence of an optimal aspect ratio region, arising from the trade-off between improved heat transfer in flatter geometries and the additional pressure drop incurred in longer beds.

However, the remarkable performance gap observed between the two configurations, even at the optimal aspect ratio, demonstrates that desorption efficiency ultimately governs overall process performance. Steam injection proved to be decisive in this regard, unlocking a productivity region that is fundamentally unattainable with wall heating alone. This effect was further illustrated by extracting the minimum work–productivity envelopes, which clearly expose the expanded operating domain enabled by steam. Altogether, the results highlight the substantial potential that can be realized by directly addressing the critical bottlenecks of the DAC-TVSA process.

Ultimately, we believe that accelerating the economic feasibility of large-scale DAC deployment requires not only the development of more performant sorbents but also the introduction of innovative design concepts. Recently, increasing attention in the literature was gained by Joule-heating technologies, as a promising alternative to conventional wall heating. For instance, Verougstraete et al. reviewed the application of electrothermal swing adsorption in structured adsorbents, highlighting the potential of monoliths and fiber cloths to achieve rapid and homogeneous heating with reduced energy losses.[59] In parallel, Lee et al. demonstrated sorbent-coated carbon fibers capable of direct Joule heating, reaching desorption temperatures within one minute and enabling rapid regeneration with competitive projected costs.[60] Moreover, newly efficient geometries are currently investigated and proposed. For instance, recent works have explored triply periodic minimal surface (TPMS) geometries as advanced gas–solid contactors for DAC,[61] as well as monolithic contactors with helical channels designed to enhance gas mixing and improve CO_2 transport.[62]

Such approaches could directly target the key bottlenecks identified in this work, offering viable alternatives to conventional pre-heating and desorption strategies while paving the way toward achieving the performance required for a worldwide deployment of DAC technologies.

Author contributions

Mattia Galanti: conceptualization, data curation, formal analysis, investigation, methodology, software, visualization, writing – original draft, and project administration; Kiia Kaaresvirta: data curation, investigation, and visualization; Ivo Roghair: resources, supervision, and writing – review and editing; Martin van Sint Annaland: resources, supervision, and writing – review and editing.

Conflicts of interest

There are no conflicts to declare.

Data availability

The data supporting this article have been included as part of the supplementary information (SI). Supplementary information is available. See DOI: https://doi.org/10.1039/d5ya00336a.

Acknowledgements

Notes and references

1 WGI Summary for Policymakers Headline Statements|Climate Change 2021: The Physical Science Basis, 2021, https://www.ipcc.ch/report/ar6/wg1/resources/spm-headline-statements/.
2 Net Zero by 2050 – Analysis – IEA, 2021, https://www.iea.org/reports/net-zero-by-2050.
3 G. Luderer, Z. Vrontisi, C. Bertram, O. Y. Edelenbosch, R. C. Pietzcker, J. Rogelj, H. S. De Boer, L. Drouet, J. Emmerling, O. Fricko, S. Fujimori, P. Havlík, G. Iyer, K. Keramidas, A. Kitous, M. Pehl, V. Krey, K. Riahi, B. Saveyn, M. Tavoni, D. P. Van Vuuren and E. Kriegler, Nat. Clim. Change, 2018, 8(7), 626–633.
4 J. Rogelj, G. Luderer, R. C. Pietzcker, E. Kriegler, M. Schaeffer, V. Krey and K. Riahi, Nat. Clim. Change, 2015, 5, 519–527.
5 M. Zeeshan, M. K. Kidder, E. Pentzer, R. B. Getman and B. Gurkan, Front. Sustainability, 2023, 4, 1167713.
6 M. Ozkan, S. P. Nayak, A. D. Ruiz and W. Jiang, iScience, 2022, 25, 103990.
7 M. Erans, E. S. Sanz-Pérez, D. P. Hanak, Z. Clulow, D. M. Reiner and G. A. Mutch, Energy Environ. Sci., 2022, 15, 1360–1405.
8 A. Sodiq, Y. Abdullatif, B. Aissa, A. Ostovar, N. Nassar, M. El-Naas and A. Amhamed, Environ. Technol. Innovation, 2023, 29, 102991.
9 Direct Air Capture 2022 – Analysis – IEA, 2022, https://www.iea.org/reports/direct-air-capture-2022.
10 CCUS – Analysis – IEA, https://www.iea.org/reports/ccus.
11 H. Bouaboula, J. Chaouki, Y. Belmabkhout and A. Zaabout, Chem. Eng. J., 2024, 484, 149411.
12 F. Sabatino, A. Grimm, F. Gallucci, M. van Sint Annaland, G. J. Kramer and M. Gazzani, Joule, 2021, 5, 2047–2076.
13 LEWATIT® VP OC 1065, https://lanxess.com/en/products-and-brands/products/l/lewatit-vp-oc-1065.
14 R. Veneman, N. Frigka, W. Zhao, Z. Li, S. Kersten and W. Brilman, Int. J. Greenhouse Gas Control, 2015, 41, 268–275.
15 S. Sutanto, J. W. Dijkstra, J. A. Pieterse, J. Boon, P. Hauwert and D. W. Brilman, Sep. Purif. Technol., 2017, 184, 12–25.
16 M. J. Bos, T. Kreuger, S. R. Kersten and D. W. Brilman, Chem. Eng. J., 2019, 377, 120374.
17 J. Young, E. García-Díez, S. Garcia and M. Van Der Spek, Energy Environ. Sci., 2021, 14, 5377–5394.
18 M. Y. A. Low, D. Danaci, H. Azzan, R. T. Woodward and C. Petit, J. Chem. Eng. Data, 2023, 68, 3499–3511.
19 W. Shi, S. Chen, R. Xie, A. Gonzalez-Diaz, X. Zhang, T. Wang and L. Jiang, Chem. Eng. J., 2024, 496, 154090.
20 S. B. Petersen, E. M. L. Sánchez and T. H. Pedersen, Sustainable Energy Fuels, 2025, 9, 879–890.
21 D. Marinič and B. Likozar, J. Cleaner Prod., 2023, 408, 137185.
22 M. Galanti, R. Teunissen, I. Roghair and M. van Sint Annaland, Curr. Opin. Chem. Eng., 2026, 51, 101201.
23 S. H. Leenders, G. Pankratova, J. Wijenberg, J. Romanuka, F. Gharavi, J. Tsou, M. Infantino, L. van Haandel, S. van Paasen and P. E. Just, ChemSusChem, 2023, 16, e202300930.
24 D. D. Duong, Adsorption analysis: equilibria and kinetics, Imperial College Press, 1st edn, 1998, vol. 3.
25 N. S. Wilkins, J. A. Sawada and A. Rajendran, J. Chem. Eng. Data, 2024, 69, 1781–1803.
26 M. Thommes, K. Kaneko, A. V. Neimark, J. P. Olivier, F. Rodriguez-Reinoso, J. Rouquerol and K. S. Sing, Pure Appl. Chem., 2015, 87, 1051–1069.
27 I. Portugal, V. M. Dias, R. F. Duarte and D. V. Evtuguin, J. Phys. Chem. B, 2010, 114, 4047–4055.
28 R. B. Anderson, J. Am. Chem. Soc., 1946, 68, 686–691.
29 W. Wagner and A. Pruß, J. Phys. Chem. Ref. Data, 2002, 31, 387–535.
30 M. Shan, Y. Jin, F. M. Chimani, A. A. Bhandari, A. Wallmüller, G. Schöny, S. Müller and J. Fuchs, Separations, 2024, 11, 160.
31 A. Y. Song, J. Young, J. Wang, S. N. Fricke, K. Piscina, R. Giovine, S. Garcia, M. van der Spek and J. A. Reimer, J. Mater. Chem. A, 2024, 12, 25875–25886.
32 K. Piscina and M. Van der Spek, New insights into the swelling of amine-functionalised adsorbents for direct air CO$_2$ capture, Proceedings of the 17th greenhouse gas control technologies conference (GHGT-17) 2024, available at, DOI: 10.2139/ssrn.5065640.
33 V. Stampi-Bombelli, M. van der Spek and M. Mazzotti, Adsorption, 2020, 26, 1183–1197.
34 A. Ward, M. M. Papathanasiou and R. Pini, Adsorption, 2024, 30, 1829–1848.
35 B. M. Balasubramaniam, P. T. Thierry, S. Lethier, V. Pugnet, P. Llewellyn and A. Rajendran, Chem. Eng. J., 2024, 485, 149568.

36 L. Jiang, W. Liu, R. Q. Wang, A. Gonzalez-Diaz, M. F. Rojas-Michaga, S. Michailos, M. Pourkashanian, X. J. Zhang and C. Font-Palma, *Prog. Energy Combust. Sci.*, 2023, **95**, 101069.

37 H. M. Schellevis, T. N. van Schagen and D. W. Brilman, *Int. J. Greenhouse Gas Control*, 2021, **110**, 103431.

38 G. Christoph, R. Nicolas and W. Jan Andre, *Steam assisted vacuum desorption process for carbon dioxide capture*, 2015.

39 S. M. Wilson, *Sep. Purif. Technol.*, 2022, **294**, 121186.

40 *The Atmosphere|National Oceanic and Atmospheric Administration*, 2024, https://www.noaa.gov/jetstream/atmosphere.

41 E. Glueckauf, *Formula for diffusion into spheres ad their applications to chromatography*, Atomic energy research establishment technical report, 1955.

42 S. Sircar and J. R. Hufton, *Adsorption*, 2000, **6**, 137–147.

43 S. Sircar and J. R. Hufton, *AIChE J.*, 2000, **46**, 659–660.

44 Y. Wang, D. Zhao and G. K. Li, *Adsorption*, 2025, **31**, 1–13.

45 M. Y. A. Low, D. Danaci, C. Sturman and C. Petit, *Chem. Eng. Res. Des.*, 2025, **215**, 443–452.

46 A. G. Dixon and D. L. Cresswell, *AIChE J.*, 1979, **25**, 663–676.

47 A. G. Dixon, *Chem. Eng. Process.*, 1996, **35**, 323–331.

48 A. G. Dixon, *Can. J. Chem. Eng.*, 2012, **90**, 507–527.

49 E. Peters and M. van Sint Annaland, *pymrm: Python package for Multiphase Reactor Modeling*, 2025, DOI: 10.5281/zenodo.17069860.

50 A. C. Hindmarsh, P. N. Brown, K. E. Grant, S. L. Lee, R. Serban, D. E. Shumaker and C. S. Woodward, *ACM Trans. Math. Software*, 2005, **31**, 363–396.

51 D. J. Gardner, D. R. Reynolds, C. S. Woodward and C. J. Balos, *ACM Trans. Math. Software*, 2022, **48**, 1–24.

52 C. R. Randall, scikit-SUNDAE: Python bindings to SUNDIALS Differential Algebraic Equation solvers [SWR-24-137], 2024, https://github.com/NREL/scikit-sundae.

53 D. Danaci, P. A. Webley and C. Petit, *Front. Chem. Eng.*, 2020, **2**, 602430.

54 *Aramis CCS|Homepage*, https://www.aramis-ccs.com/.

55 *Aramis CCS|CO2 specifications for Aramis transport infrastructure*, https://www.aramis-ccs.com/news/co2-specifications-for-aramis-transport-infrastructure/.

56 K. Deb, A. Pratap, S. Agarwal and T. Meyarivan, *IEEE Trans. Evol. Comput.*, 2002, **6**, 182–197.

57 J. Blank and K. Deb, *IEEE Access*, 2020, **8**, 89497–89509.

58 K. Deb, K. Sindhya and T. Okabe, *Proceedings of GECCO 2007: Genetic and Evolutionary Computation Conference*, 2007, pp. 1187–1194.

59 B. Verougstraete, M. Gholami, Y. Gomez-Rueda, E. Pérez-Botella, M. Schoukens, T. R. Van Assche and J. F. Denayer, *Sep. Purif. Technol.*, 2025, **353**, 128522.

60 W. H. Lee, X. Zhang, S. Banerjee, C. W. Jones, M. J. Realff and R. P. Lively, *Joule*, 2023, **7**, 1241–1259.

61 S. Y. Kim, H. E. Holmes, Y. Wang, S. C. Weston and R. P. Lively, *Adv. Funct. Mater.*, 2025, **35**, 2410356.

62 E. Tegeler, Y. Cui, M. Masoudi, A. M. Bahmanpour, T. Colbert, J. Hensel and V. Balakotaiah, *Chem. Eng. Sci.*, 2023, **281**, 119107.